

Article

Some Peculiarities of Low-Frequency Hydroacoustic Signals Behavior in Tomographic Studies of “Sea-Land-Sea” System

Sergey Budrin * , Grigory Dolgikh , Vladimir Chupin  and Stanislav Dolgikh 

V.I. Il'ichev Pacific Oceanological Institute, Far Eastern Branch Russian Academy of Sciences,
690041 Vladivostok, Russia

* Correspondence: ss_budrin@mail.ru

Abstract: In this paper, we analyzed the results of experimental data processing in the study of regularities of propagation and transformation of low-frequency harmonic signals at the boundary of the “sea–land–sea” system. Harmonic signals at a carrier frequency of 33 Hz were generated by a low-frequency hydroacoustic radiator in Vityaz Bay. Then, they passed along the shelf of decreasing depth, transformed into seismoacoustic signals of the upper layer of the Earth’s crust and the bedrocks of Shultz Cape and excited hydroacoustic signals at the corresponding frequency in the shelf waters in the open part of the Sea of Japan. When processing the experiment results, we obtained the vertical distributions of the pressure field, caused by an acoustic low-frequency signal passing through the upper layer of the Earth’s crust. We presented the distributions of hydroacoustic and seismoacoustic energies. The obtained experimental data were compared with the simulations by the model, developed strictly according to the experiment scheme and the geological structure of the area. In the discussion of the obtained results, we explained a probable mechanism of acoustic energy propagation and the nature of the vertical distributions of the pressure field formation.

Keywords: low-frequency hydroacoustic radiator; laser strainmeter; acoustic tomography; seismoacoustic; hydrophone system



Citation: Budrin, S.; Dolgikh, G.; Chupin, V.; Dolgikh, S. Some Peculiarities of Low-Frequency Hydroacoustic Signals Behavior in Tomographic Studies of “Sea-Land-Sea” System. *J. Mar. Sci. Eng.* **2022**, *10*, 1550. <https://doi.org/10.3390/jmse10101550>

Academic Editor: Rouseff Daniel

Received: 14 September 2022

Accepted: 18 October 2022

Published: 20 October 2022

Publisher’s Note: MDPI stays neutral with regard to jurisdictional claims in published maps and institutional affiliations.



Copyright: © 2022 by the authors. Licensee MDPI, Basel, Switzerland. This article is an open access article distributed under the terms and conditions of the Creative Commons Attribution (CC BY) license (<https://creativecommons.org/licenses/by/4.0/>).

1. Introduction

Acoustic tomography methods were originally developed for monitoring deep ocean areas and studying their dynamic characteristics [1]. Conventionally, acoustic tomography methods can be divided into two kinds: active and passive methods.

In [2], a classical implementation of acoustic tomography active methods is presented, with the hardware part that includes seven autonomous receiving-transmitting systems operating at a frequency of 50 kHz and located at depths of up to 100 m. In addition to the receiver and transmitter, each station is equipped with pressure sensors that control the depth of immersion and allow measuring tide parameters. GPS receivers, installed at each station, are used to synchronize the measurements. Near each point, acoustic Doppler current profilers (ADCPs) are installed on the bottom to measure currents and environmental parameters in the study area and also CTD sondes that measure salinity, temperature, and pressure. The data are transmitted to the shore via a radio channel.

As noted above, in addition to acoustic tomography active methods, there are also passive ones. For example, the works [3,4] describe a method of passive acoustic tomography, where passing ships are used as radiation sources. This system consists of freely drifting radio buoys with suspended hydrophones. The positions of ships are controlled by the automatic identification system (AIS), and the positions of the buoys are monitored by GPS receivers. Thus, the delay time of the sound signal, associated with hydrophysical processes, is calculated. The paper presents the results of experiments, conducted off the coast of New London, Connecticut, in Long Island Sound in August 2015. Various signals of natural origin, such as seismic signals, can be used as sources of radiation.

In both passive and active methods of acoustic tomography, various receiving systems and complexes are used. In the original method, an ocean glider [5] is the carrier of receiving systems. Currently, gliders are widely used to collect hydrophysical parameters of the environment such as temperature and salinity, which in turn are useful for acoustic tomography. If an acoustic receiver is placed on a glider, it can become a part of a tomographic system that provides additional information on time of acoustic rays' propagation. However, there are problems associated with use of gliders as acoustic receivers, for example, uncertainty in the submerged position, which can lead to uncertainty in the received data.

Recently, in connection with development of shelf zones water areas, solutions to the problem of monitoring various parameters of shallow sea have become interesting. In contrast to deep ocean, in the shelf zone, the seabed strongly influences the characteristics of the acoustic field, which makes it necessary to know the parameters of the seabed. Therefore, reconstruction of shallow sea bottom parameters to address such problems can be of separate interest and can be used to identify geological structures of the shelf area. The indisputable advantage of tomographic methods is the possibility of studying the entire space of a water area of many kilometers and remote reconstruction of the seabed parameters. In all these experiments, the receiving systems were located on the bottom or, as a maximum, were frozen into ice.

The works [6,7] present another method of acoustic tomography of shallow water areas, including those covered with ice, which is aimed at studying not only the main parameters of water environment, but also the structure and composition of the upper layer of the sea Earth's crust in the studied water areas. Radiating hydroacoustic systems operating at frequencies of 22, 33, and 245 Hz are located in the water at various distances from the receiving systems, including a towed option, and the receiving systems are located on the shore. In these works, laser strainmeters with unique amplitude–frequency characteristics are used as receiving systems [8,9]. Low-frequency hydroacoustic radiators [10,11], which were used in experiments, generated signals of various complexities, including harmonic and phase-manipulated signals. Phase-manipulated signals were used to solve tomographic problems, and harmonic signals were used to study the regularities of propagation and transformation of hydroacoustic signals in shallow sea and at the boundaries of the “atmosphere–hydrosphere–lithosphere” system. Based on the results of each experiment, we designed models of the seabed structure at the experimental site and, on the base of these models, carried out studies of the recorded seismic waves' time characteristics.

To successfully solve the tomographic problems of shallow sea, we need to know, first of all, regularities of propagation and transformation of low-frequency hydroacoustic signals on a shelf of varying depth, with a complex seabed structure. For this purpose, experimental studies were carried out with low-frequency hydroacoustic radiators as transmitting systems and hydroacoustic complexes and coastal laser strainmeters as receiving systems for hydroacoustic signals and transformed seismoacoustic signals [12,13]. These experiments were carried out according to the same scheme: radiation was given out in water on the shelf of decreasing depth, transmitted hydroacoustic signals were received in selected points of the shelf at different depths, and transformed seismoacoustic signals were received by a coastal laser strainmeter.

The paper [14] describes an experiment with completely different schemes: seismoacoustic signals were generated by a low-frequency seismoacoustic radiator onshore, their registration was performed by a laser strainmeter, and a reception of transformed hydroacoustic signals was performed in water by receiving hydroacoustic systems.

From the above, we can formulate several important issues related to the conduct of the experiment, described in this paper, i.e., generation of low-frequency hydroacoustic signals in a practically closed reservoir; transformation of hydroacoustic signals into seismoacoustic, with their further propagation over various land layers; transformation of seismoacoustic signals into hydroacoustic signals, with their further propagation over the shelf of increasing depth.

2. Experiment Description

In the experiment presented in the paper, a low-frequency hydroacoustic radiator of electrodynamic type was used as a transmitting source, generating a “forward-scattering” tone signal [10]. The maximum overpressure at a resonant frequency of 33 Hz, created by the radiator on the acoustic axis at a distance of 1 m, reached 2.2 kPa.

To receive hydroacoustic signals in water, we used an autonomous submersible container, consisting of an 8104 hydrophone by Brüel and Kjær, brought outside through a sealed connection, a NEXUS 2692 charge amplifier by the same manufacturer, and a hard disk recording system. The hydrophone had a sensitivity of 56 $\mu\text{V}/\text{Pa}$ and could receive signals in the frequency range from 0.1 Hz to 120 kHz. The charge amplifier had built-in low-pass and high-pass filters and could amplify from -20 to $+80$ dB, with a sensor capacitance of 1 nF. During the experiment, we used a filter, built into the amplifier, with cutoff frequencies of 10 and 100 Hz, which allowed us to receive a 33 Hz tone signal and avoid unwanted noise in the low-frequency range. The frame, where the hydrophone was fixed, was covered with a mesh, which helped avoid noise of hydrodynamic characteristics. Using an analog-to-digital converter, the data from the charge amplifier were recorded by a portable computer. An accumulator bank was used in a container as a power source, ensuring autonomy of all devices up to 9 h.

Registration of seismoacoustic signals, generated by the radiator, was carried out using a coastal laser strainmeter, built on the basis of an unequal-arm Michelson interferometer. The length of the strainmeter arm was 52.5 m. A frequency-stabilized laser with a wavelength of 630 nm was used as a radiation source. Theoretically, the laser strainmeter can measure a displacement with an accuracy of $(\lambda_l/2) \times 10^{-6}$, where λ_l is the wavelength of the frequency-stabilized laser. At a displacement measurement accuracy of 0.01 nm, the sensitivity of the 52.5 m laser strainmeter was equal to $(\Delta L/L) = (0.01 \text{ nm}/52.5 \text{ m})$ [9].

Figure 1 shows a scheme map of the experiment.



Figure 1. Scheme map of the experiment. The “radiator” was the transmitting point; P1–P5 were measurement points.

Transmitting signals was carried out in Vityaz Bay of the Peter the Great Gulf. The radiator was submerged to the depth of 18 m, while the depth of sea at the radiation point was 25 m. Hydroacoustic signals were transformed into seismoacoustic signals and were recorded by the coastal laser strainmeter. After passing through Shultz Cape, seismoacoustic signals continued to propagate along the wedge-shaped shelf and partially transformed back into hydroacoustic signals, which were measured in several points (P1–P4) on the side of the open part of the Sea of Japan.

Radiation of tone signals with a frequency of 33 Hz was carried out in the continuous mode. In the measurement points, we measured sound velocities over the entire depth using a hydrological sonde. Then, the autonomous submersible hydroacoustic container equipped with a hydrophone measured, at intervals of 2 m from the surface to the bottom, the pressure field created by hydroacoustic signals, which was formed by seismoacoustic signals that passed through Shultz Cape.

After the experiment and the analysis of the obtained experimental data, we carried out the mathematical modeling of the process of acoustic signal propagation along the route “water-the upper layer of the Earth’s crust-water”. The model parameters fully corresponded to the experimental conditions. After that, we compared the obtained experimental data and simulation results.

3. Description and Parameters of the Model

To estimate the distribution of the pressure field, generated by acoustic signals as they propagated in a layered elastic medium and in an overlying fluid medium, we performed modeling, using an axisymmetric code of spectral elements in the time domain. The modeling tool was the spectral element method, which is a high-order finite element method, developed for local- and global-scale seismic waves’ propagation [15]. Acoustic signal propagation on the shelf with a decreasing depth was modeled using the SEM software package with the SPECFEM2D open source [16,17].

SPECFEM2D integrates a simplified form of the wave by Equations (1)–(3), using high-degree Lagrange interpolation polynomials. In spatially inhomogeneous region of fluid, the wave equation for the pressure $P(x,t)$ has the following form:

$$\frac{1}{k} \ddot{P} = \nabla \left(\frac{\nabla P}{\rho} \right), \tag{1}$$

where $k(x)$ is the adiabatic fluid bulk modulus.

In linearly elastic bodies, the strain tensor $\varepsilon(x,t)$ is calculated from the displacement vector u as:

$$\varepsilon = \frac{1}{2} (\nabla \vec{u} + [\nabla \vec{u}]^T). \tag{2}$$

The stress tensor $\vec{\sigma}(\vec{x}, t)$ can be expressed in terms of the strain tensor, according to Hooke’s law:

$$\vec{\sigma} = \vec{c} : \varepsilon, \tag{3}$$

where colon denotes the double tensor contraction operation. The elastic properties of the medium are described by the fourth-order elasticity tensor $c(x)$. SPECFEM2D integrates a simplified form of these equations, using a high-degree polynomial Lagrange approximation.

The simulation parameters are shown in Figure 2. The surface of the fluid medium was set at $z = 0$. The radiation source was set by the Ricker function with a central frequency of 33 Hz and was located in the point with coordinates $(r,z) = (0, -18 \text{ m})$. The calculation area had a width of 3100 m and a depth of 500 m below the sea surface. All boundaries, except for the upper one, were defined by perfectly matched layers (PMLs) [18]. In order to obtain accurate results of wave propagation simulations using SPECFEM2D, it is necessary to specify a mesh with an element size equal to the smallest wavelength. In this case, the element size was taken to be $\sim 30 \text{ m}$. The model mesh was created using the open-source software Gmsh [19] and consisted of 3145 spectral elements. The physical parameters of the shelf geological structure are listed in Table 1.

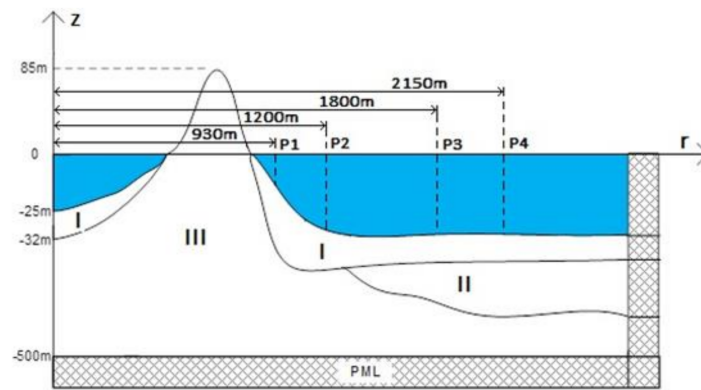


Figure 2. Simulation parameters.

Table 1. Parameters of geological layers used in the model.

Layer	c_p	c_s	Specific Gravity
I–Late Pleistocene Holocene	1740 m/s	1044 m/s	1.5 g/sm ³
II–Gelasian Middle Pleistocene	1880 m/s	1128 m/s	1.7 g/sm ³
III–Granites	3790 m/s	2274 m/s	2.4 g/sm ³

4. Processing of the Experimental Data Comparison with the Simulation by the Model

As we mentioned above, hydroacoustic signal measurements in each point were carried out at intervals of 2 m. According to the obtained values of the overpressure, measured at each horizon, we plotted the curves of the vertical distribution of the pressure field vs. depth. With the same depths and intervals, according to the model, the same distributions were calculated for all measurement points. The construction results are shown in Figure 3.

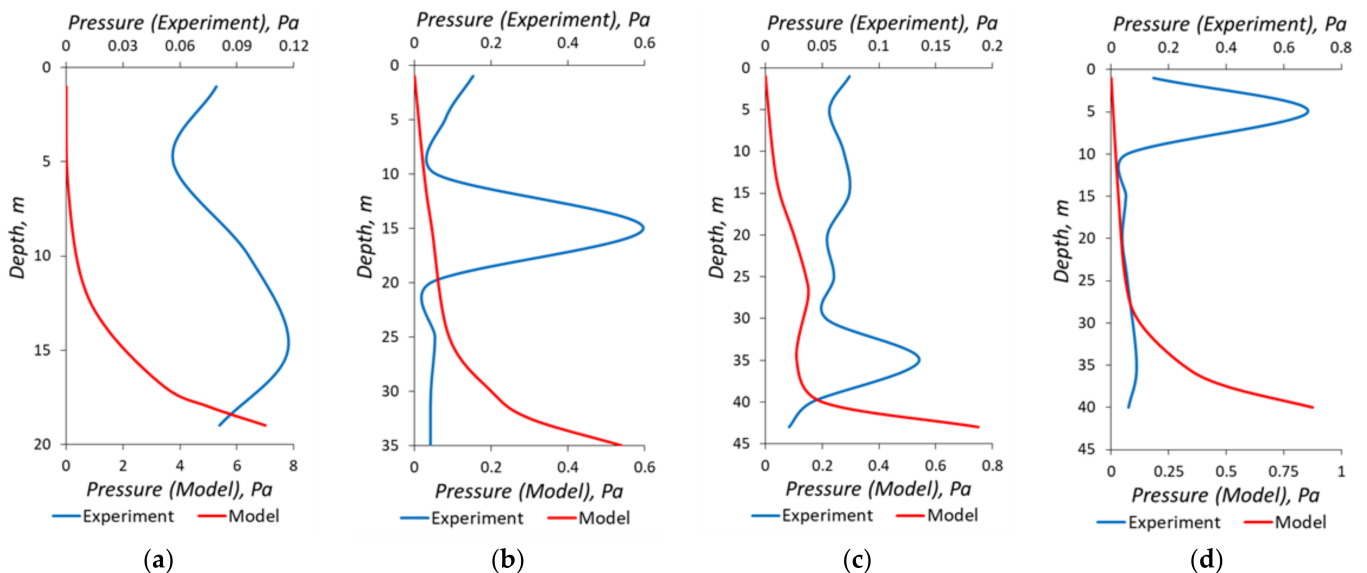


Figure 3. Vertical distributions of the pressure field, measured and calculated by the model at points: (a) P1; (b) P2; (c) P3; (d) P4.

The graphs built on the simulation data were practically identical. The maximum of the pressure field was located near the bottom, which was expected, since it was assumed that the acoustic signal that passed through the cape would subsequently propagate through the upper layer of sedimentary rocks (Figure 2(I)), create the maximum pressure near the bottom, and decay exponentially towards the surface. However, the curves constructed

from the experimental data were starkly different from the model. In Figure 3a, the main maximum of the pressure field was at the depth of about 15 m. In the measurement point P2 at a distance of 1200 m from the radiator (Figure 3b), we can observe the maximum at the same depth, but with a much larger amplitude. In points P3 and P4, located at the distances of 1800 and 2150 m from the radiator, the situation changed dramatically. In Figure 3d, the distribution of the pressure field was not uniform in depth and the maximum was located near the bottom, while at point P4 (Figure 3c), the maximum of the pressure field was located near the surface. An interesting feature in all cases was the “channeling” of the pressure field in 10 m thick layers.

5. Analysis of Energy Parameters of Oscillations in Solid and Fluid Media

By distributions of the pressure field and the signal, recorded by the laser strainmeter, we calculated the specific hydroacoustic and seismoacoustic energies for each measurement point.

The energy density of a hydroacoustic field in a fluid medium can be calculated using the following expression:

$$E_w(h) = \frac{1}{2\rho c^2} \int_0^h P(h)^2 dh, \tag{4}$$

where ρ is the water density, c is the sound velocity in water, h is the depth in the measurement point, and $P(h)$ is the pressure distribution function over depth.

The expression for calculating the energy density of elastic oscillations in a solid medium can be written as:

$$E_r(h) = \int_0^\lambda \frac{\rho\omega^2 u^2 \exp(-4\pi/\lambda)}{2 \cos(\theta)^2} dz, \tag{5}$$

where u is the displacement amplitude at a frequency of 33 Hz, recorded by the laser strainmeter, λ is the Rayleigh wavelength ($c = 3790$ m/s), ρ is the density of the upper layer of the Earth’s crust (2400 kg/m³), θ is the angle between the measuring axis of the laser strainmeter and the direction to the radiator (4.5 deg), and ω is the cyclic frequency for $f = 33$ Hz.

All calculation results are listed in Table 2. Figure 4 shows a mutual comparison of the obtained results in a graphical form.

Figure 4b shows that the change in hydroacoustic energy occurred in a non-trivial way, the maxima form at the distances of 1200 and 2150 m from the radiator. The energy distribution according to the model, on the contrary, had a classical exponential characteristic, with the exception of a small maximum at the distance of 1800 m from the radiator, which is most likely associated with appearance of the third layer in the geological structure of the shelf (Figure 2(II)). Absolutely unclear is the nature of the change in seismoacoustic energy, which is possibly associated with the unstable operation of the radiator, but this does not explain the presence of the hydroacoustic energy maxima at the minimum of seismoacoustic energy.

Table 2. Seismoacoustic and hydroacoustic energy densities.

Point No.	Depth (m)	Distance from the Radiator (m)	Displacement Amplitude (m)	Seismoacoustic Energy Density (J/m ³)	Hydroacoustic Energy Density by Experiment (J/m ³)	Hydroacoustic Energy Density by the Model (J/m ³)
P1	19	930	4.34×10^{-9}	8.94×10^{-9}	6.79×10^{-11}	3.44×10^{-8}
P2	35	1200	1.95×10^{-9}	1.85×10^{-9}	5.30×10^{-10}	3.27×10^{-10}
P3	43	1800	2.88×10^{-9}	3.94×10^{-9}	9.63×10^{-11}	2.35×10^{-9}
P4	41	2150	4.44×10^{-9}	9.36×10^{-9}	1.00×10^{-9}	9.29×10^{-10}

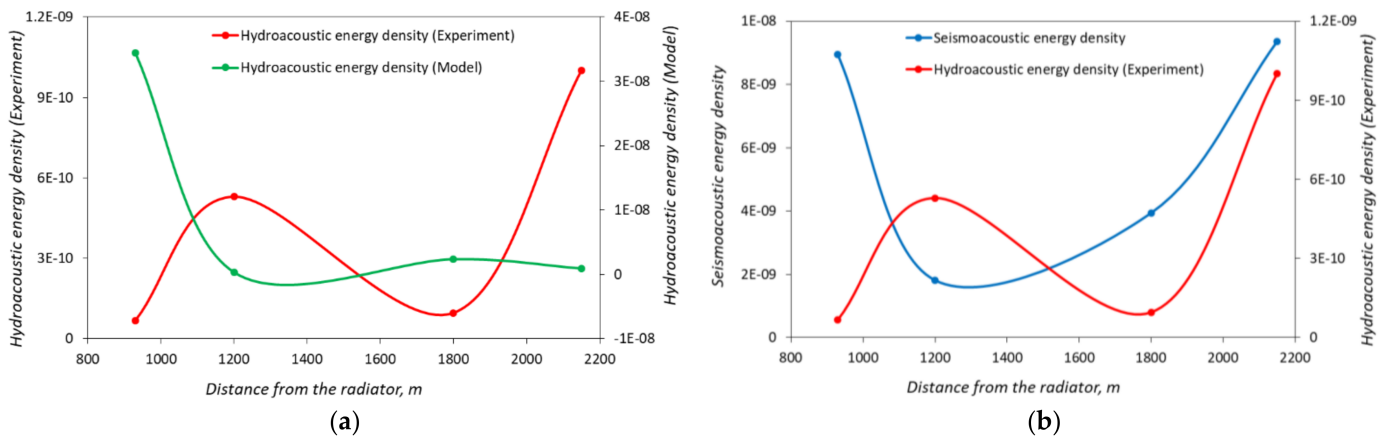


Figure 4. (a) Comparison of the energy densities of oscillations recorded by the laser strainmeter and the energy densities of the experimentally measured hydroacoustic signals; (b) comparison of energy density values of elastic oscillations: energy density of the experimentally measured hydroacoustic signals and energy densities calculated according to the model.

We calculated ratios of hydroacoustic and seismoacoustic energies from point to point. The energies at the first point were considered as units, and ratios were further calculated by dividing the energy at a point by the energy at the next one. The calculation results are listed in Table 3, and they are presented in a graphical form in Figure 5.

Table 3. Ratios of seismoacoustic and hydroacoustic energy densities, calculated from point to point.

Type of Energy Density	P1/P1	P1/P2	P2/P3	P3/P4
Hydroacoustic energy density change	1	0.12816157	5.500415282	0.096223776
Seismoacoustic energy density change	1	4.925619835	0.460543009	0.421091997

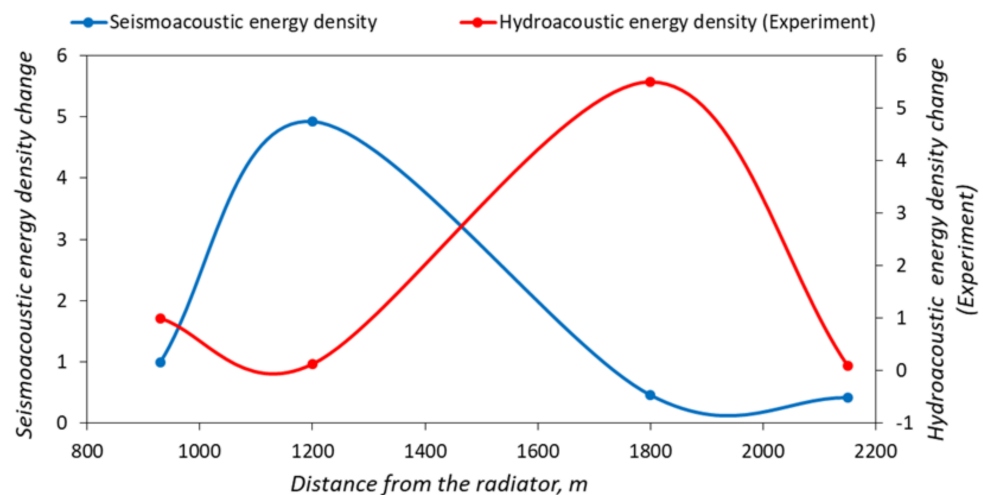


Figure 5. Changes in hydroacoustic and seismoacoustic energy densities from point to point.

Basing on the graphs of energy variations, we can instantly say that they were interconnected and inversely proportional to each other. This means that with an increase in seismoacoustic energy, less energy entered the fluid half-space, and vice versa. The smaller the energy change in the solid half-space, the more the energy entering the fluid medium.

6. Discussion of the Obtained Results

From the above, we can make some assumptions on the mechanism of the pressure field distributions formation, presented in Figure 3. The first assumption is related to the

presence of hydrophysical processes, such as internal waves, during the experiment. This assumption is hardly probable, since at each point, we measured the hydrological sonde sound velocity and the temperature over depth. Figure 6 shows the vertical distributions of the sound velocity and the temperature for two points.

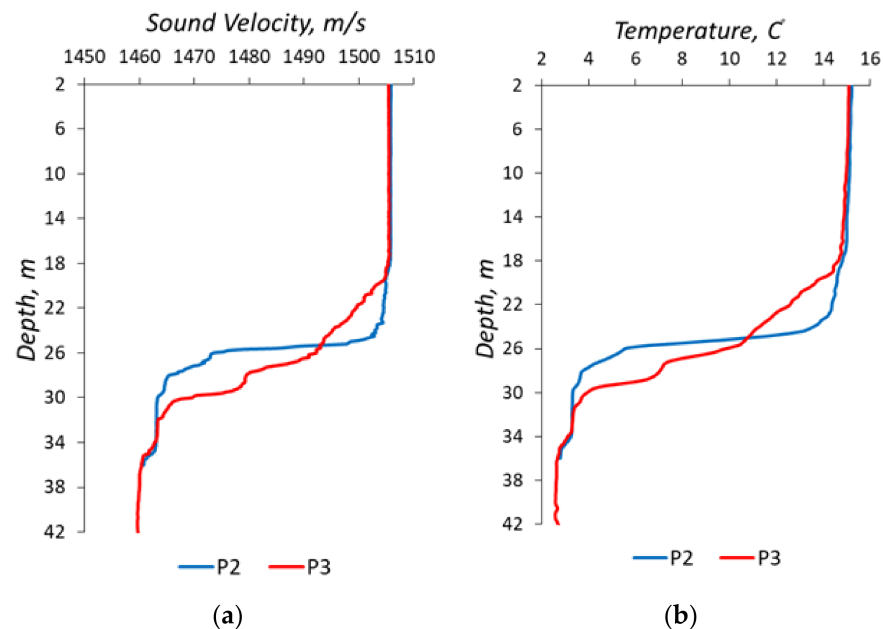


Figure 6. Vertical distributions of the sound velocity (a) and the temperature (b) at measurement points P2 and P3.

According to the distributions presented in Figure 6, small negative gradients of the sound velocity and the temperature were formed in the 18–22 m thick upper layer. Then, there was a 10–12 m thick transition layer, after which there was also a small negative gradient.

The assumption of existence of some internal or surface channels of acoustic energy propagation is also inconsistent, since the wavelength of the harmonic signal that we used was commensurable with the depth at the measurement points, and, therefore, the transition layer, in this case, did not matter much.

Based on the above, we can make an assumption about the mechanism of acoustic signal transmission from one shelf area to another through the solid half-space. Let us examine the mechanism of transformation of acoustic energy from the radiator into the upper layer of the Earth's crust. As shown by the results of our previous experiments [12,13], 90% of acoustic energy goes into the bottom immediately. The rest of the energy gradually transforms with the decrease in depth and completely goes into the bottom when the critical depth is reached. Therefore, we can assume that at the first two measurement points, the distribution of the pressure field was formed by the energy that went into the bottom directly at the critical depth and passed directly through the solid half-space (Schulz Cape). The main part of the energy, which went into the bottom, immediately propagated deeper in the granite base (Figure 2(III)) and began to come to the surface with an appearance of sedimentary rocks in the geological structure (Figure 2(I,II)). At points P3 and P4, the pressure field was formed as a result of interaction of straight energy passing "through" and the energy exiting into the fluid half-space, which made the structure of the pressure field distribution over depth inhomogeneous.

Let us examine the distributions of the pressure fields at points P1 and P2 (Figure 3a,b). We were interested in the pressure change from the surface to the bottom at stations P1 and P2. As we noted above, at these stations, the maximum pressure was at the depth of 15 m. In addition, we should note that, when compared with the simulated data, the pressure

increased near the surface at both stations. This growth can be associated, as in [13], with the existence of an undamped Rayleigh-type wave at the “water-bottom” boundary. If the amplitude of a damped Rayleigh wave decreased exponentially from the bottom to the water surface, then amplitude of an undamped wave did not decrease from the bottom to the surface. The superposition of these amplitudes provided such a behavior of the total pressure at the frequency of 33 Hz from the depths of 5–8 m to the surface. More interesting is the fact that at these stations the maximum pressure was at the depth of 15 m. According to the model, presented in Figure 2, the main component of the rocks of Schultz Cape is bedrocks with a velocity of longitudinal waves of about 3790 m/s [13]. The layer thicknesses to the left and to the right of Schultz Cape are small at shallow depths. Taking into account the hydroacoustic wave length, this layer cannot significantly affect the behavior of hydroacoustic waves at the “water-bottom” boundary. Bedrocks provide the main influence. Taking this fact into account, we can calculate the critical depth, at which hydroacoustic energy, propagating along the wedge-shaped shelf of decreasing depth, is almost completely transformed into seismoacoustic energy. According to [13], the critical depth was calculated as follows:

$$H = \frac{c}{4f\sqrt{1-n^2}}, \quad (6)$$

where c is the sound velocity in water, n is the refraction index equal to the ratio of the sound velocity in water to the sound velocity in the seabed, and f is 33 Hz. For the parameters described above, this critical depth was approximately equal to 12.4 m, which was slightly less than 15 m. For the critical depth of 15 m, the sound velocity in the seabed should be approximately equal to 2300 m/s. This is quite possible, taking into account the layered and heterogeneous structure of the upper layer of the Earth’s crust at the experimental site. Therefore, we can assume that the critical depth, at which all hydroacoustic energy is transformed into seismoacoustic energy, can be from 12.4 to 15 m. We suppose that the concentrations of energy at the first two points were associated with the critical depth, at which the transformed seismoacoustic energy converted back into hydroacoustic energy, and this critical depth was 15 m. We can even consider the seabed area from the water edge near the coast to the second receiving point as an antenna, radiating hydroacoustic energy, the main lobe of which is at the critical depth of 15 m. At the first receiving station, the total hydroacoustic energy was lower by almost an order of magnitude than at the second receiving station. This may be not only due to the possibly unstable operation of the radiator, but also due to the “inefficient” operation of the radiating seismoacoustic antenna with the “bottom-water” boundary starting from the depth of 17 m to the water edge. The tilt of this radiating seismoacoustic antenna was about 60°. At the third and fourth receiving stations, the picture is much more complicated. Here, body waves, which immediately went into the bottom in the radiation area, begin to play an important role. In the points of reception, these waves, when entering the water, should be “superimposed” on damped and undamped hydroacoustic Rayleigh-type waves. This interaction of waves gives such pressure distributions. In this case, the maximum pressure can be at any depth from the surface of the water to the bottom.

We can estimate the stability of the radiator operation by the seismoacoustic energy, received by the laser strainmeter. In this case, we should take into account that during the experiment, both radiating and receiving systems (laser strainmeter) were stationary. This instability can only be associated with the presence of surface waves during the experiment. In the presence of wind waves, the radiator moved either to or away from the bottom. This led to the change in the ratio of energy, which went into the bottom in the form of body waves, to the hydroacoustic energy, which transformed into seismoacoustic energy in the form of surface waves. At such small distances from the place of the radiator operation to the laser strainmeter, the latter recorded only surface waves.

7. Conclusions

Thus, we can conclude that the formation of vertical distributions of the pressure field directly depends on the shape and geological structure of the shelf area, and experiments with use of low-frequency harmonic signals allow us to obtain comprehensive information on transmission mechanisms and propagation paths of acoustic energy when a signal passes through a solid half-space bounded by water environment. This type of experiment can later be used to create an acoustic tomography method that will make it possible to study the geological structure of the shelf areas of the World Ocean, including those in hard-to-reach areas covered with ice.

Besides, under certain conditions, we can generate very powerful seismoacoustic signals of varying complexity, for example phase-manipulated signals, using hydroacoustic low-frequency radiators that generate powerful signals of varying complexity. These studies are important not only for solving a number of tomographic problems, but also for developing new methods of navigation and communication. In the future, such experiments are extremely necessary at large distances to solve the problems of constructing a model of the hydroacoustic field of the shelf area as the depth increases, depending on the structure and composition of the sea Earth's crust.

Author Contributions: Conceptualization, G.D.; methodology, G.D.; formal analysis, G.D., S.B., S.D. and V.C.; data curation, S.B., S.D. and V.C.; writing—original draft preparation, G.D., S.B., S.D. and V.C.; writing—review and editing, G.D., S.B., S.D. and V.C.; visualization, S.B., S.D. and V.C.; project administration, G.D. All authors have read and agreed to the published version of the manuscript.

Funding: The research was carried out as a part of the Russian State assignment No. AAAA-A20-120021990003-3 on the topic "Study of the fundamental basis of the origin, development, transformation, and interaction of hydroacoustical, hydrophysical, and geophysical fields of the World Ocean".

Institutional Review Board Statement: Not applicable.

Informed Consent Statement: Not applicable.

Data Availability Statement: Not applicable.

Conflicts of Interest: The authors declare no conflict of interest. The funders had no role in the design of the study; in the collection, analyses, or interpretation of data; in the writing of the manuscript; or in the decision to publish the results.

References

1. Munk, W.H.; Worcester, P.F.; Wunsch, C. *Ocean Acoustic Tomography*, 2nd ed.; Cambridge University Press: New York, NY, USA, 1995; p. 447. ISBN 0521470951.
2. Kaneko, A.; Zhu, X.; Lin, J. *Coastal Acoustic Tomography*, 1st ed.; Elsevier: Amsterdam, The Netherlands, 2020; p. 362, ISBN 9780128189429.
3. Bruce, C.; William, A.K.; William, S.H.; Jeff, T.; Jit, S.; Christopher, M.V.; Karim, G.S. Passive travel time tomography using ships as acoustic sources of opportunity. *J. Acoust. Soc. Am.* **2016**, *140*, 3074. [[CrossRef](#)]
4. Jacquelyn, S.K.; Christopher, M.V.; Brendan, V.N.; Karim, G.S. Passive ocean acoustic tomography using ships as sources of opportunity recorded on an irregularly spaced free-floating array: A feasibility study. *J. Acoust. Soc. Am.* **2016**, *139*, 2026. [[CrossRef](#)]
5. Van Uffelen, L.J.; Sarah, E.W.; Craig, M.L.; Jason, I.G.; Peter, F.W.; Matthew, A.D. Ocean gliders as tools for acoustic tomography. *J. Acoust. Soc. Am.* **2016**, *140*, 3075. [[CrossRef](#)]
6. Dolgikh, G.I.; Dolgikh, S.G.; Pivovarov, A.A.; Samchenko, A.N.; Chupin, V.A.; Shvyryov, A.N.; Yaroshchuk, I.O. The feasibility of laser strainmeters for sea floor diagnostics. *Dokl. Earth Sci.* **2013**, *452*, 971–975. [[CrossRef](#)]
7. Dolgikh, G.I.; Budrin, S.S.; Dolgikh, S.G.; Ovcharenko, V.V.; Pivovarov, A.A.; Samchenko, A.N.; Shvyrev, A.N.; Chupin, V.A.; Yaroshchuk, I.O. Development of tomographic technology for the Earth's crust in the shelf regions. *Dokl. Earth Sci.* **2017**, *475*, 811–815. [[CrossRef](#)]
8. Dolgikh, G.I.; Kovalev, S.N.; Koren', I.A.; Ovcharenko, V.V. A Two-Coordinate Laser Strainmeter. *Izv. Phys. Sol. Earth.* **1998**, *34*, 946–950. [[CrossRef](#)]
9. Dolgikh, G.I. Principles of designing single-coordinate laser strainmeters. *Tech. Phys. Lett.* **2011**, *37*, 204–206. [[CrossRef](#)]
10. Dolgikh, G.I.; Yaroshchuk, I.O.; Pivovarov, A.A.; Penkin, S.I.; Shvyrev, A.N. Low-frequency broadband hydroacoustic radiation system. *Instrum. Exp. Technol.* **2007**, *5*, 163–164. [[CrossRef](#)]

11. Dolgikh, G.I.; Dolgikh, S.G.; Pivovarov, A.A. A Hydroacoustic System that Radiates at Frequencies of 19–26 Hz. *Instrum. Exp. Technol.* **2017**, *60*, 596–600. [[CrossRef](#)]
12. Dolgikh, G.I.; Budrin, S.S.; Dolgikh, S.G.; Ovcharenko, V.V.; Chupin, V.A.; Yakovenko, S.V. Particulars of a transmitted acoustic signal at the shelf of decreasing depth. *J. Acoust. Soc. Am.* **2017**, *142*, 1990–1996. [[CrossRef](#)] [[PubMed](#)]
13. Dolgikh, G.I.; Budrin, S.S.; Dolgikh, S.G.; Chupin, V.A.; Yakovenko, S.V.; Piao, S.; Song, Y.; Dong, Y.; Wang, X. Study of low-frequency hydroacoustic waves behavior at the shelf of decreasing depth. *Appl. Sci.* **2020**, *10*, 3183. [[CrossRef](#)]
14. Dolgikh, G.I.; Batyushin, G.N.; Dolgikh, S.G.; Dzyuba, V.P.; Chupin, V.A. Transformation of Seismoacoustic Energy into Hydroacoustic. *Dokl. Earth Sci.* **2008**, *423*, 1514–1515. [[CrossRef](#)]
15. Bottero, A.; Cristini, P.; Komatitsch, D.; Asch, M. An axisymmetric time-domain spectral-element method for full-wave simulations: Application to ocean acoustics. *J. Acoust. Soc. Am.* **2016**, *140*, 3520–3530. [[CrossRef](#)] [[PubMed](#)]
16. Komatitsch, D.; Tromp, J. Introduction to the spectral-element method for 3-D seismic wave propagation. *Geophys. J. Int.* **1999**, *139*, 806–822. [[CrossRef](#)]
17. Cristini, P.; Komatitsch, D. Some illustrative examples of the use of a spectral-element method in ocean acoustics. *J. Acoust. Soc. Am.* **2012**, *131*, 229–235. [[CrossRef](#)] [[PubMed](#)]
18. Xie, Z.; Matzen, R.; Cristini, P.; Komatitsch, D.; Martin, R. A perfectly matched layer for fluid-solid problems: Application to oceanacoustics simulations with solid ocean bottoms. *J. Acoust. Soc. Am.* **2016**, *140*, 165–175. [[CrossRef](#)] [[PubMed](#)]
19. Geuzaine, C.; Remacle, J.F. Gmsh: A 3-D finite element mesh generator with built-in pre- and post-processing facilities. *Int. J. Numer. Meth. Eng.* **2009**, *79*, 1309–1331. [[CrossRef](#)]